The new

ALFOSC Camera

equipped with E2V CCD42-40-1-B83, ser. no. 01064-17-06
Pre-commissioning characterisation

Anton Norup Sørensen
Copenhagen University Observatory

September 2003

Contents

1 Introduction

This report presents the pre-commissioning characterisation results of the upgraded detector for ALFOSC. The CCD is now a E2V CCD42-40-1-B83, ser. no. 01064-17-06, while the previous detector was the Loral-Lesser W19-(0,0). Both detectors are back-side illuminated with 2048^2 imaging pixels and two read-out channels. The new CCD offers improved performance in read-out-noise and image sharpness. The improvement in image quality is in part due to better camera optics, and in part because of less charge diffusion in the detector. The pixel size of the new detector is only $13.5\mu m$ square, while the Loral has $15\mu m$ pixels. The image scale and field size is unchanged, as the new optics compensates for this difference.

The performance described here is measured in the laboratory of Copenhagen University Observatory. The liquid Nitrogen cryostat to be used for the assembled camera is the same as for the previous camera, and was present at NOT during the tests at CUO. The tests were in stead made using a closed-cycle-cooler cryostat.

2 Cosmetics

Flat fields at wavelengths of 1060nm, 550nm and 334nm are shown in figure 1

In the central optical band, around 550nm, uniformity is very good, with a typical structure amplitude of $\pm 0.5\%$. A stitching pattern is visible as three horisontal lines, but this flat fields out fine. Some shadows from dust specks on the test dewar window can be seen. Spots with low sensitivity are very few, in contrast to Loral CCDs.

At the longest wavelengths, uniformity is poorer, with large scale variations at the $\pm 4\%$ level. This is slightly better than found on Loral CCDs. The variatios seem to be related to reflecting layers below the sensitive layer. At the bottom, fans of light are reflected off the bonding wires.

At 334nm, a highly regular pattern appears, probably from a laser annealing process. The amplitude of the pattern is about $\pm 5\%$, and on top is a large scale pattern of similar amplitude. This leaves the short wavelength response rather uneven.

A similar measure of flat field quality is the Pixel Response Non-Uniformity (PRNU). This was determined for a 400 by 400 pixel segment along with QE measurements, and is displayed as vertical bars in figure 10. Worst PRNU of 2.4% is found at the shortest wavelength of 334nm. It then improves in the visual band, where typical PRNU is 0.6%, an degrades slightly in the near-IR to about 1%. The values are in agreement with the E2V test sheet results.

Charge traps and bad columns can be found by comparing a flat field exposure at very low illumination level to a well exposed one, as illustrated in figure 2. Several exposures at $17e^-$ and $42Ke^-$ were combined to produce two high S/N flat field maps for the comparison.

In the table below, the coordinates of defects found are listed. Trap depth is estimated from the approximation that depth equals the number of affected pixels multiplied by the exposure level. The actual trap location is the smallest Y-coordinate of the area.

Low level traps	**Comment**
$[462, 927 : 1135]$	$3Ke^-$
$[909, 905 : 935]$	$500e^-$
$[368, 1]$	
$[680, 1]$	
$[833, 1]$	
$[926, 1]$	
$[1705, 1 : 5]$	$100e^-$
$[2061, 1]$	
$[2077, 1]$	

Two traps are present in the imaging area, while several weak traps ($< 50e^-$) are seen at the interface between the imaging area and the serial register. Only some of the strongest interface

traps are listed here. A close-up of some of the register traps are seen in figure 3, along with their effect on a Fe-55 CTE exposure.

The test sheet from E2V gives a trap count of only one. E2V defines a trap as having a capacity of at least 200e$^-$ at -30°C. As this test is performed at -120°C and our trap depth estimate is rather crude, the results are not necessarily conflicting with the E2V findings.

3 Read-out noise

The detector voltages were modified to optimise read-out noise (RON) without compromising linearity, and gain was adjusted to avoid influence from quantisation noise in high-gain mode. The following table shows the resulting RON found in different amplifier configurations.

	Amplifier A	Amplifier B
High gain:	$3.25 \pm 0.05e^-$	$3.75 \pm 0.05e^-$
Low gain:	$3.7 \pm 0.1e^-$	$4.2 \pm 0.1e^-$

The test sheet from E2V gives 3.2 e$^-$ in A and 3.3 e$^-$ in B. A slight pattern from electronic pick-up noise was visible when using amplifier B, and this probably accounts for the difference in the measured RON. Low-gain RON is higher due to a stronger impact from quantisation noise.

4 Cross-talk

In dual read-out mode, cross-talk can occur between the two output circuits. An image of a star in one side of the image will then have a faint electronic ghost image mirrored around the border of the two image sections.

A pin-hole was imaged in one channel, at an illumination level of several times the blooming full well. The image was then sought for in the opposite channel, with ten exposures summed in order to detect faint features.

For both channels, no ghost image was detected. If the performance of the individual outputs are considered acceptable, there appears to be no problems in utilizing dual read-out mode.

5 Gain, linearity and full-well

Gain, the conversion factor from Analog to Digital Units (ADU) and electrons was determined in two ways: By analysis of photon noise statistics, and by illumination with Fe-55 X-rays of known energy. The following conversion factors were found:

	Amplifier A	Amplifier B
High gain, Poisson:	$0.76 \pm 0.01e^-$/ADU	$0.77 \pm 0.01e^-$/ADU
High gain, Fe-55:	$0.756 \pm 0.005e^-$/ADU	$0.768 \pm 0.005e^-$/ADU
Low gain, Poisson:	$1.58 \pm 0.02e^-$/ADU	$1.61 \pm 0.02e^-$/ADU

The two methods of gain determination are in good agreement.

The data for gain determination from Poisson noise are shown in the upper part of figures 4, 5, 6 and 7. Here the gain is determined from the average level measured over a wide illumination range.

Gain determination from noise analysis has proven to be too inaccurate for linearity measurements. In stead, linearity deviations are examined by measuring the ADU level versus exposure time, using a stable light source. Measurements made in this way are plotted in the lower half of the linearity figures. By dividing the counts with the exposure time, corrected for shutter delay, a linear response should result in a constant level.

- Amplifier A, high gain is linear to within ± 0.3% from 270e$^-$ to 47Ke$^-$ (360 – 63KADU).

- Amplifier B, high gain is linear to within ± 1% from 260e$^-$ to 48Ke$^-$ (330 – 63KADU). If the lowest level counts are excluded, linearity rapidly improves, e.g. it becomes linear to within ± 0.3% from 800e$^-$ and above. The low level deviation is suspected to be due to poorer bias level stability.

- Amplifier A, low gain is linear to within ± 0.6% from 270e$^-$ to 65Ke$^-$ (170 – 41KADU). A highly linear region exists between 1KADU and 40KADU. Below that, much of the deviation may be attributed to inaccurate bias level subtraction. Above 40KADU, amplifier non-linearity is severe.

- Amplifier B, low gain is linear to within ± 1.1% from 260e$^-$ to 61Ke$^-$ (160 – 38KADU). Again, linearity improves considerably if the lowest count levels are discarded. Above 38KADU, amplifier non-linearity is severe.

The full well in high gain mode is defined by the digital saturation at 2^{16}ADU, about 65KADU. In low gain, a strong deviation from linearity occurs above 60Ke$^-$, due to output amplifier behaviour. The pixel charge handling capacity is significantly higher. A precise measurement was not possible, but charge blooming appears to start at a level of 200Ke$^-$ per pixel.

6 Charge Transfer Efficiency

The fraction of electrons that are successfully moved from one pixel to another during read-out is described by the charge transfer efficiency (CTE).

The CTE has been measured using a ^{55}Fe X-ray source, whose emissions generate a specific number of photo-electrons on the CCD for each detection. The read-out counts as a function of position on the CCD can then be converted to a CTE value.

The values found at a detector temperature of $-120°C$ are:

	Amplifier A	Amplifier B
Serial CTE:	0.999990	0.999991
Parallel CTE:	0.999999	0.999998

The uncertainty on the measurements is 10^{-6}, which means that the measured CTE is the same through both amplifiers.

The serial CTE is not very good, but still at a level where it should not cause any concern.

The E2V test sheet quote a serial CTE of 0.999996 in amplifier A and 0.999999 in B, and a parallel CTE of 0.999999, all measured at $-100°C$. The higher serial CTE indicate that an improvement occur at increased temperatures.

It is interesting to note that although the Fe-55 hits were affected by traps in the serial register interface, as demonstrated earlier, the CTE is unaffected.

7 Modulation Transfer Function

The previous detector on ALFOSC suffered from severe charge diffusion between pixels, as photo-electrons meandered about in a field-free region before they were caught in the potential well of a pixel. This was one of the most important reasons for the detector replacement. The measured MTF for both detectors is shown in figure 9 for illumination wavelengths of 670nm and 830nm. In the same figure, the expected MTF due to the pixel geometry is shown. The E2V clearly performs better than the Loral CCD, and in much of the spatial frequency range very close to the theoretical limit. While the MTF of the Loral depends strongly on illumination wavelength due to the change in absorption depth, the E2V device does not show any significant dependence.

8 Quantum-efficiency

The sensitivity has been measured through 11 narrow-band filters from 334nm to 1060nm and is plotted as a solid line in figure 10. The horisontal bars on the measurement points is the FWHM of the filters used.

Also shown are the E2V 42-40 minimum specifications and the E2V test data, both for a detector temperature of $-30°C$. As we operate at $-120°C$, the near-IR QE drops below the warm data. Possibly also temperature dependent, the QE shortwards of 600nm is here measured to be better than the warm data.

The final curve on figure 10 is the QE of the Loral detector to be replaced. The Loral has slightly better visual and NIR performance, probably due to a coating optimised for longer wavelengths and larger thickness of the sensitive layer. The E2V CCD performs better at wavelengths shorter than 400nm.

Pixel Response Non-Uniformity (PRNU) was determined from the same exposures. This is shown as vertical bars in the QE graph. Note that the PRNU amplitude shown is not scaled by the QE.

9 Fringes

At long wavelengths where the detector is partially transparent, internal reflections will cause interference, making QE change rapidly with wavelength and make the local variations strong for monochromatic light. Fringes are a problem in all thinned CCDs, but as the new E2V device has a smaller thickness than the Loral previously used on ALFOSC, fringing is of more concern. An example flat field is shown in figure 11, where the E2V CCD is illuminated by 830nm monochromatic light.

To characterize the fringing behavior, flat fields were made using 670nm and 830nm lasers, and monochromator illumination spanning the range 620nm to 1050nm in steps of about 50nm and with a bandwidth of approx. 2nm. Fringe amplitude was determined the standard deviation of band-pass processed flat fields. The results are plotted in figure 12. It is evident that the monochromator fringe amplitude is much smaller than the laser fringe amplitude, due to the difference in bandwidth. The laser fringes are believed to be the best representation of narrow-band sources in the sky, and the monochromator curve can be used to mark the general dependence on wavelength.

For the Loral CCDs, only laser fringe data have been obtained. Comparing the laser fringe amplitudes, it is evident that considerably stronger fringing should be expected from the new E2V CCD. Another E2V 42-40 has been characterised earlier and displayed somewhat weaker fringes, only about 2/3 amplitude of the current device.

10 Bias and overscan

The CCD has hardware overscan regions of 50 columns at each end of the serial register. These regions should be sufficient for accurate tracking of the bias level during single and dual amplifier readout.

In addition, "extended" overscan can be used, but only for read-out windows extending to the edge of the CCD opposite of the amplifier being used, as it is generated by continued clocking and read-out after the last image column. Post-processing by BIAS will always make the extended overscan appear at the right border of the image, whatever amplifier is specified.

The bias structure in vertical direction can develop considerable gradients. During a sequence of bias exposures, the gradient may be smaller than 5 ADU, but during long exposures, it may become e.g. 25 ADU. The broad overscan regions allows for excellent tracking and correction of this structure, as demonstrated in figure 14.

An offset in the overscan level during linearity tests appeared to depend on the exposure time rather than the illumination. The bias level would change linearly with exposure time for relatively short exposures, by an amount of -0.2ADU/sec for amplifier A and -0.5ADU/sec for amplifier B for exposure times up to 100 seconds.

The bias level in amplifier B is slightly offset by the amount of counts in the pixels previously read out. In figure 13, an artificial star with a peak of 40KADU in high gain diplays a tail about 30 pixels long and a maximum depth about 10 ADU lower than the background. This effect did not appear when reading out through amplifier A.

11 Dark current

The CCD is on the "non-AIMO type, meaning that it does not invert all phases during integration to minimise dark current. This requires the detector temperature to be cooled to $-120°C$ in order to suppress the dark current sufficiently for RON-limited noise in long exposures.

From several half-hour exposures, the average dark current was determined to $0.4e^-$/pixel/hour. There is a weak structure, as can be seen in figure 14, with a somewhat elevated level near the left and right borders. No hot pixels or columns were found.

Saturation residuals

A CCD illuminated well above its charge handling capacity may produce a signal similar to dark current, declining slowly over hours, as the charge leaks out from the saturated areas. This was tested by imaging a point source onto the CCD, at a level of approximately ten times the saturation limit, producing severe vertical charge blooming. The dark current in the affected area was monitored afterwards, and no extra signal was found.

Another experiment did indicate a residual signal, though. An attempt to measure dark current at $-100°C$, gave rates of 16, 9 and $3e^-$/pix/h in three consecutive half-hour dark exposures. This is most likely due to an accidental saturation of the detector before the measurements.

12 Conclusion

The new CCD42-40 for ALFOSC has been confirmed to provide better performance than the previous CCD, especially regarding read-out-noise and charge diffusion. Also cosmetics improved, with fewer traps, no bad columns and fewer low sensitivity spots. The elimination of cross-talk makes dual read-out mode more attractive, but this requires use of output B, which does not perform quite as good as output A. Near-UV efficiency is improved by the detector and optics also, and this should give a noticeable advantage.

All this comes at a price, though. Probably the small thickness of the CCD that the good MTF possible is also responsible for a rather strong fringing in the near-infrared. Removal of the fringes will require mechanical stability of the spectrograph and careful observation and reduction procedures.

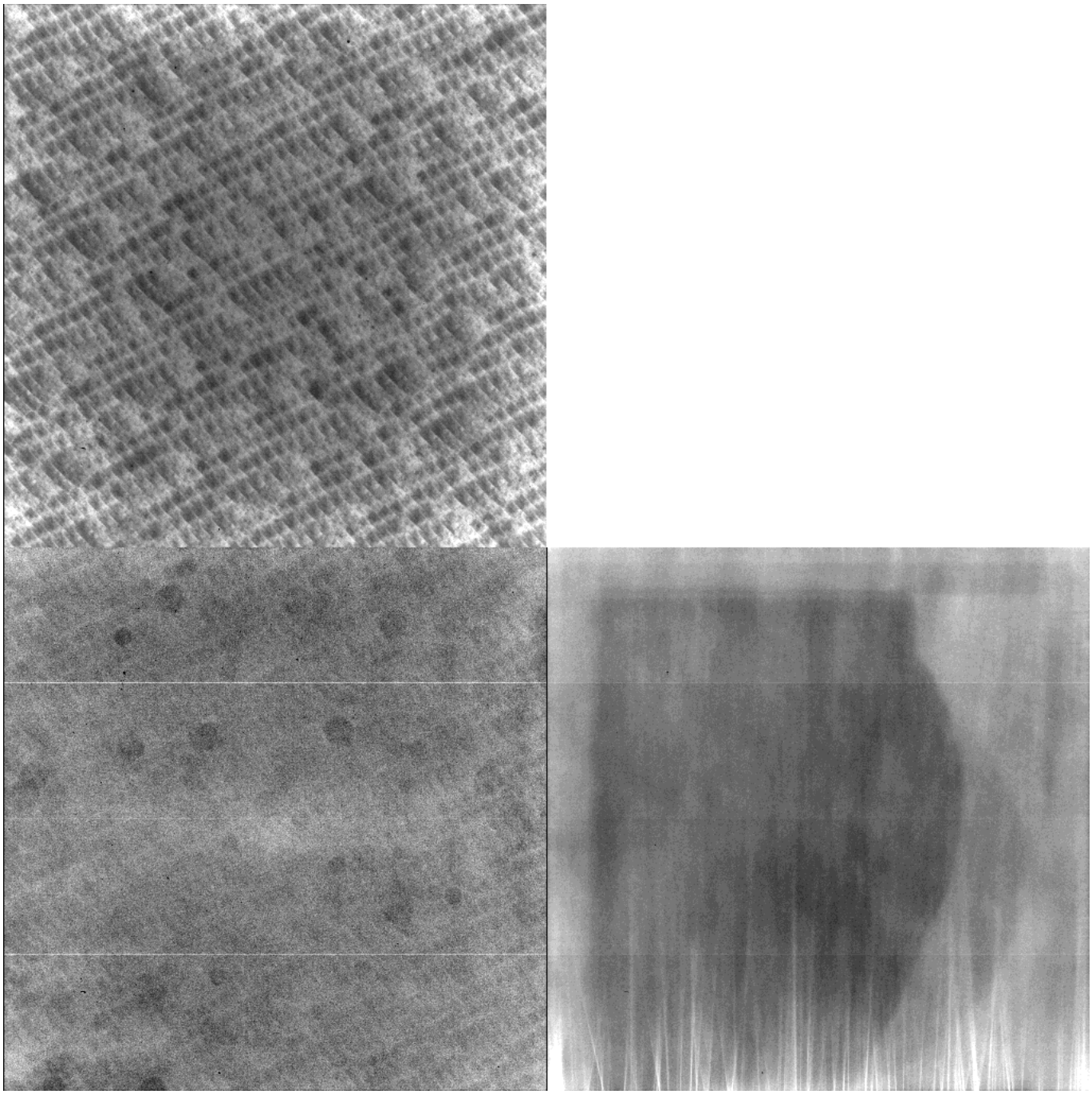

Figure 1: Flat fields at three wavelengths: *Lower left:* 550nm, with greyscale cuts set to ±2% of the median level. *Lower right:* 1060nm, with greyscale cuts of ±10%. *Top:* 334nm, with greyscale cuts of ±15%.

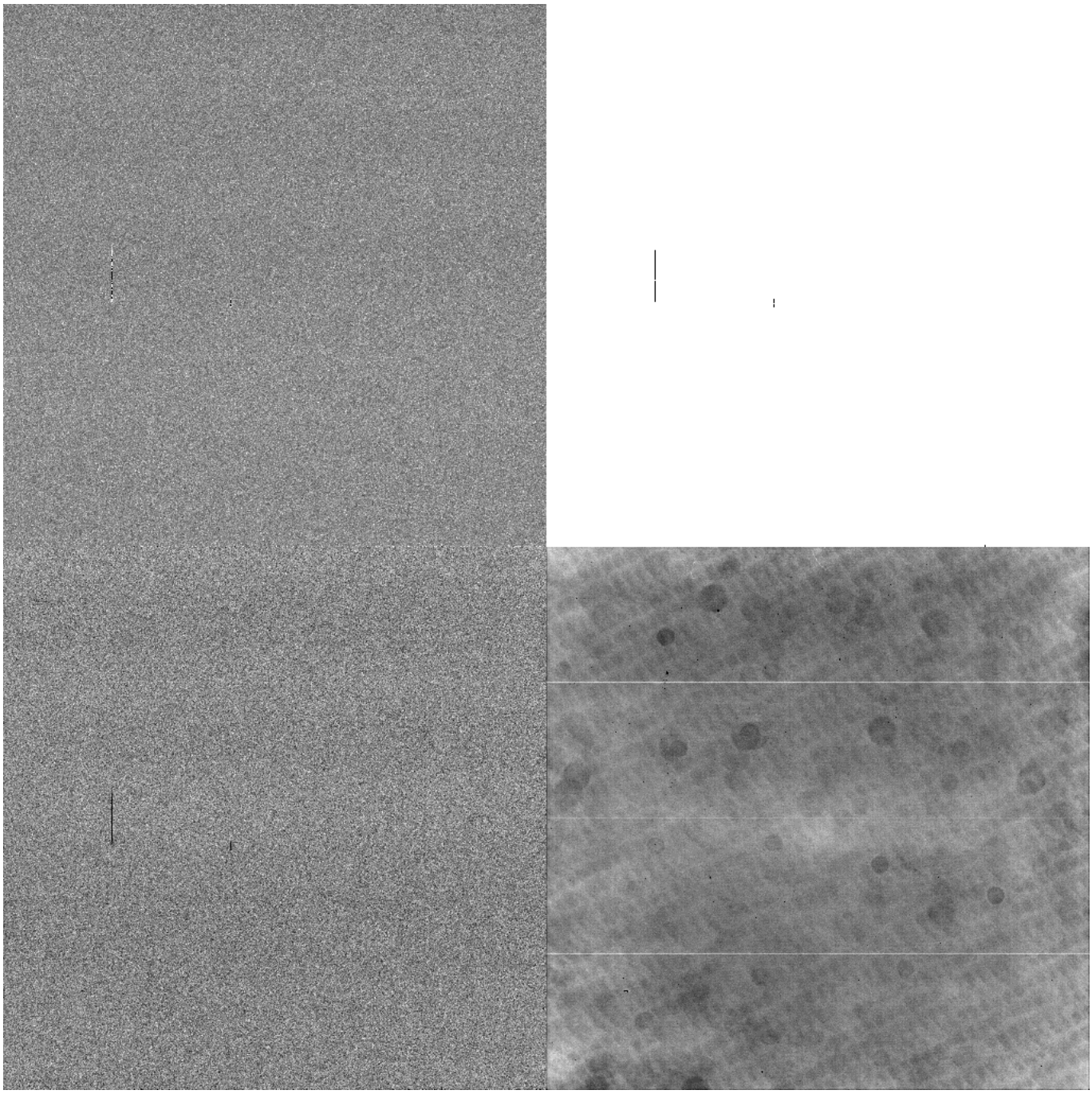

Figure 2: Low illumination level flat field properties, as a mean of identifying charge traps. *Lower left:* Flat field at an illumination level of $17e^-$/pixel. Grey scale cuts are ± 20% of median level. Signal is mostly seen as shot noise, with deep traps as dark lines. *Lower right:* Flat field at an illumination level of $42.000e^-$/pixel. Grey scale cuts are ± 2% of median level. *Upper left:* Ratio of the two flat fields. Grey scale cuts are ± 30% of median level. *Upper right:* Deviating points in the ratio image, affected by traps.

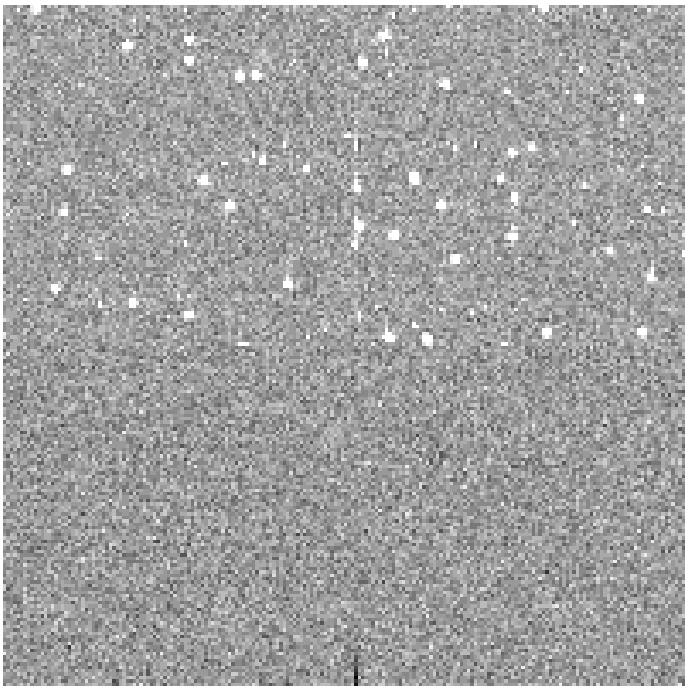

Figure 3: *Top:* Section of Fe-55 exposure. Vertical trails appear from several of the pixels. *Bottom:* Section of low-level flat field, adjacent to the serial register. The same columns are shown as in the image above. Dark columns reveal traps. Note the strong trails in the CTE exposure above the most prominent trap.

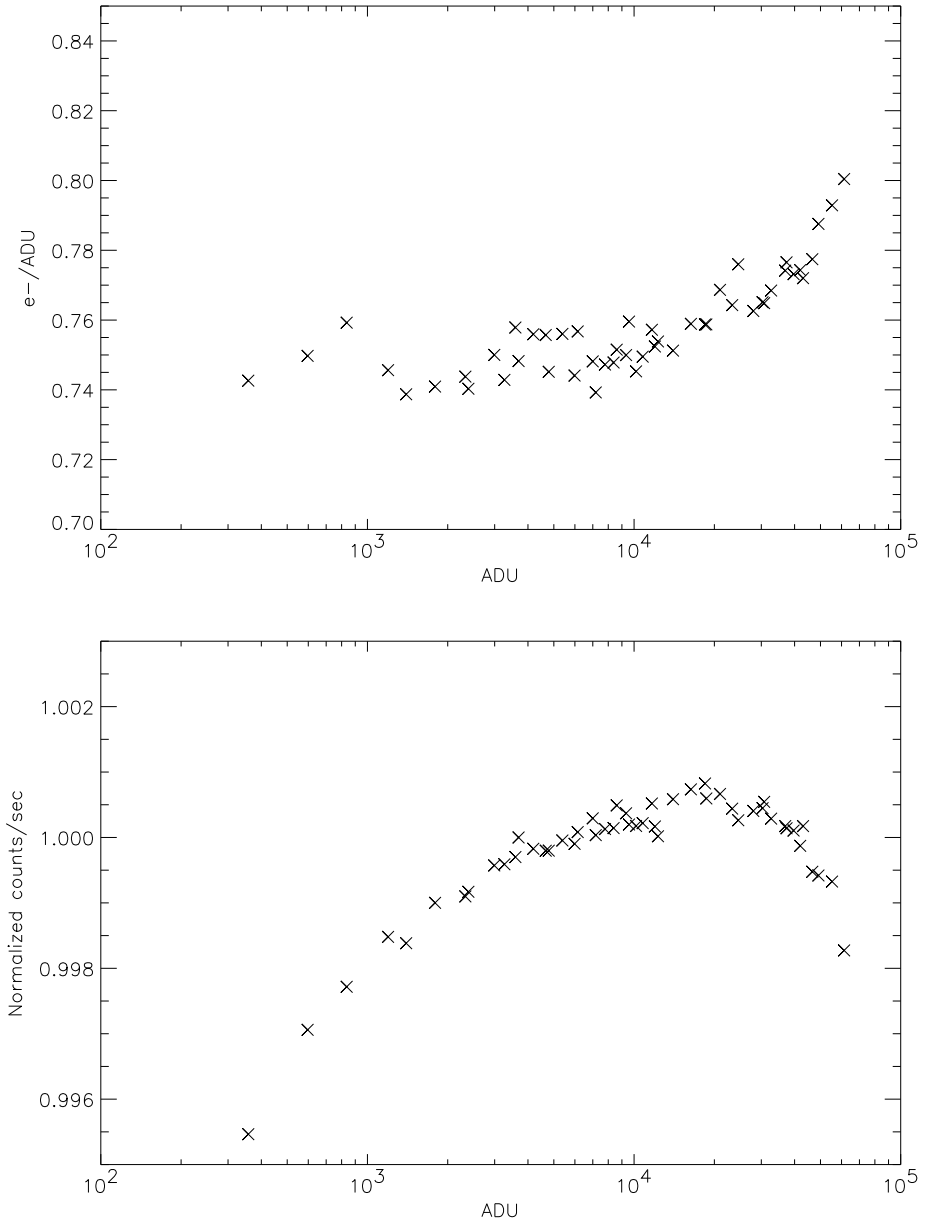

Figure 4: Linearity data for amplifier A in high gain mode. *Top:* Gain versus exposure level measured from noise statistics. *Bottom:* A plot of ADU per second versus total exposure time, corrected for shutter delay.

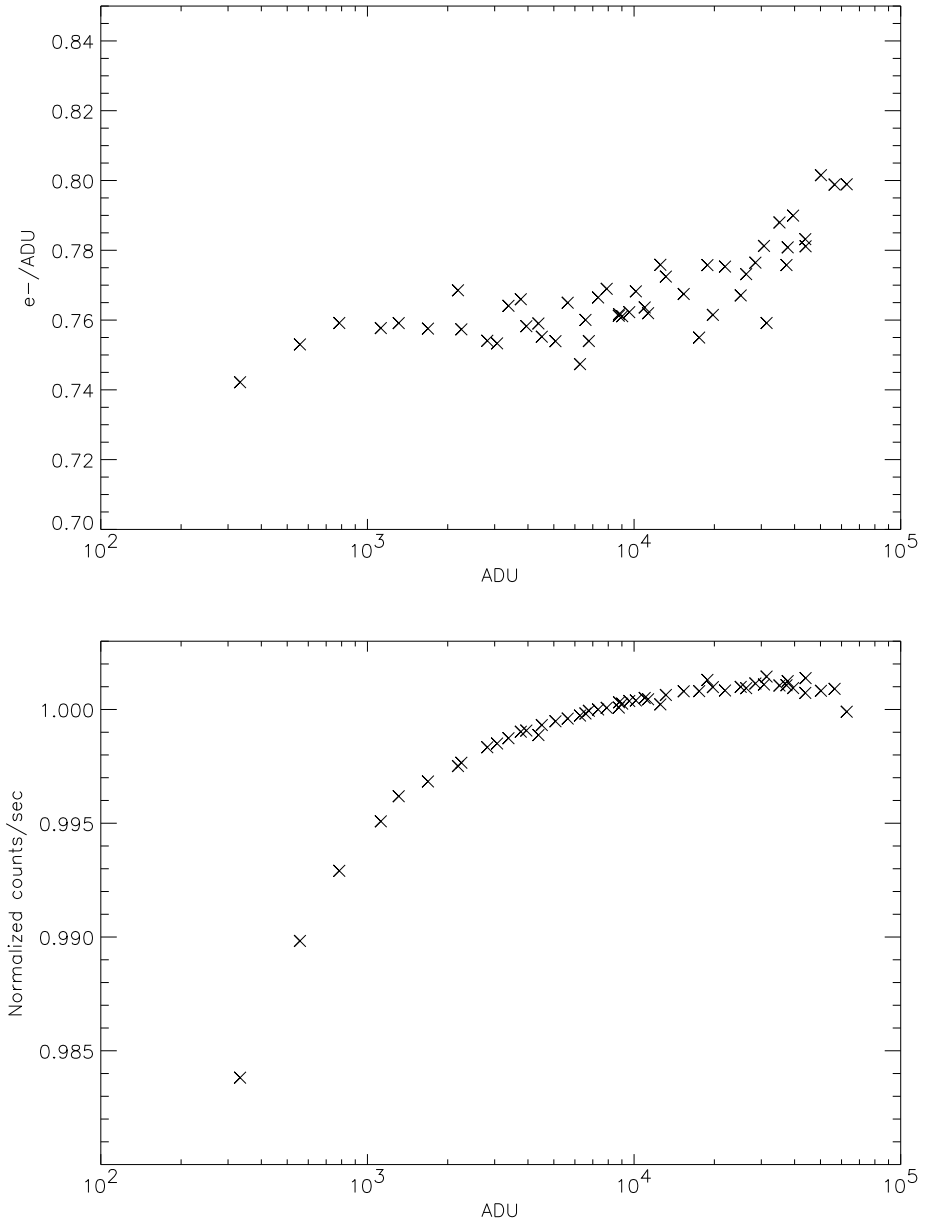

Figure 5: *Top:* Gain versus exposure level measured from noise statistics for amplifier B in high-gain mode. *Bottom:* A plot of ADU per second versus total exposure time, corrected for shutter delay. Data is again for amplifier B in high-gain mode.

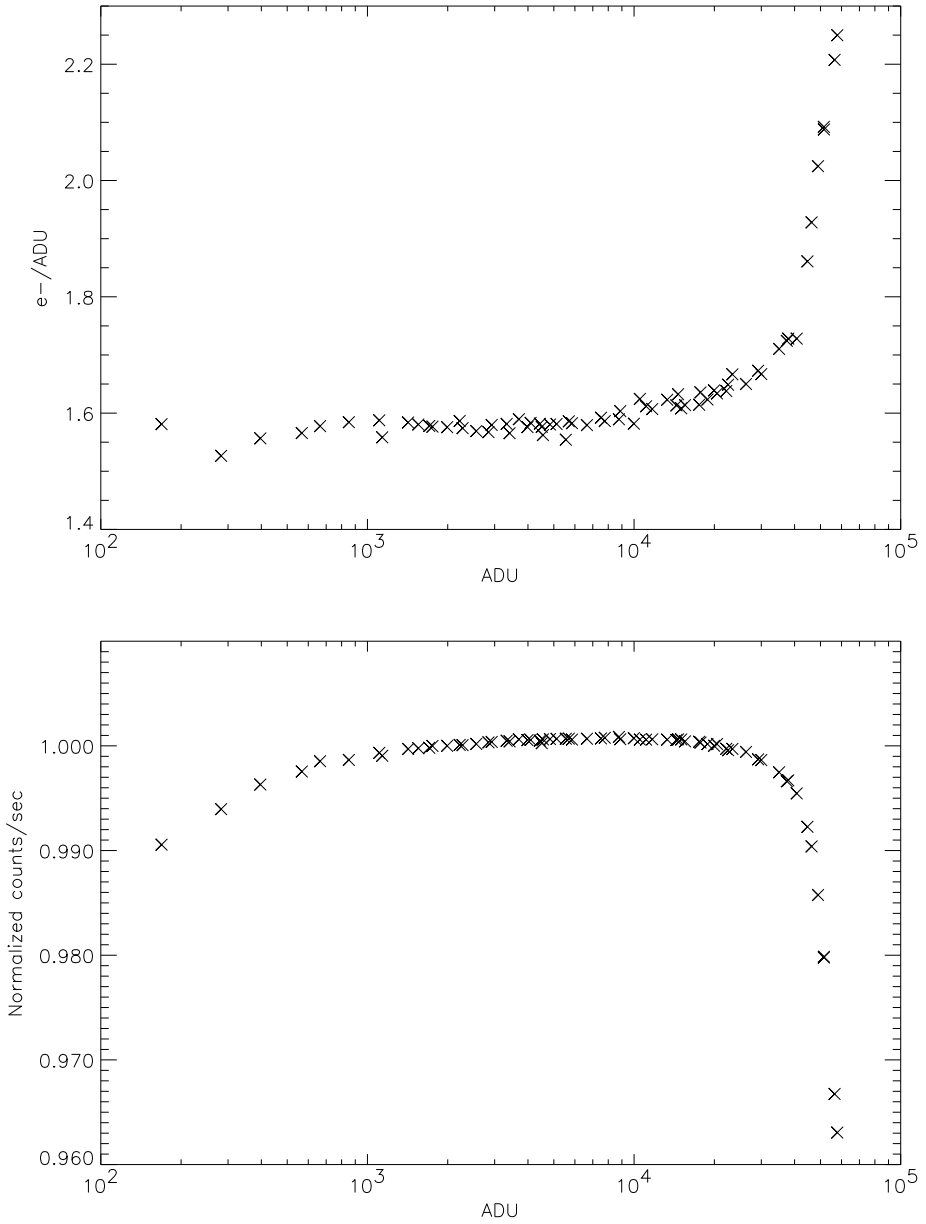

Figure 6: *Top:* Gain versus exposure level measured from noise statistics for amplifier A in low-gain mode. *Bottom:* A plot of ADU per second versus total exposure time, corrected for shutter delay. Data is again for amplifier A in low-gain mode.

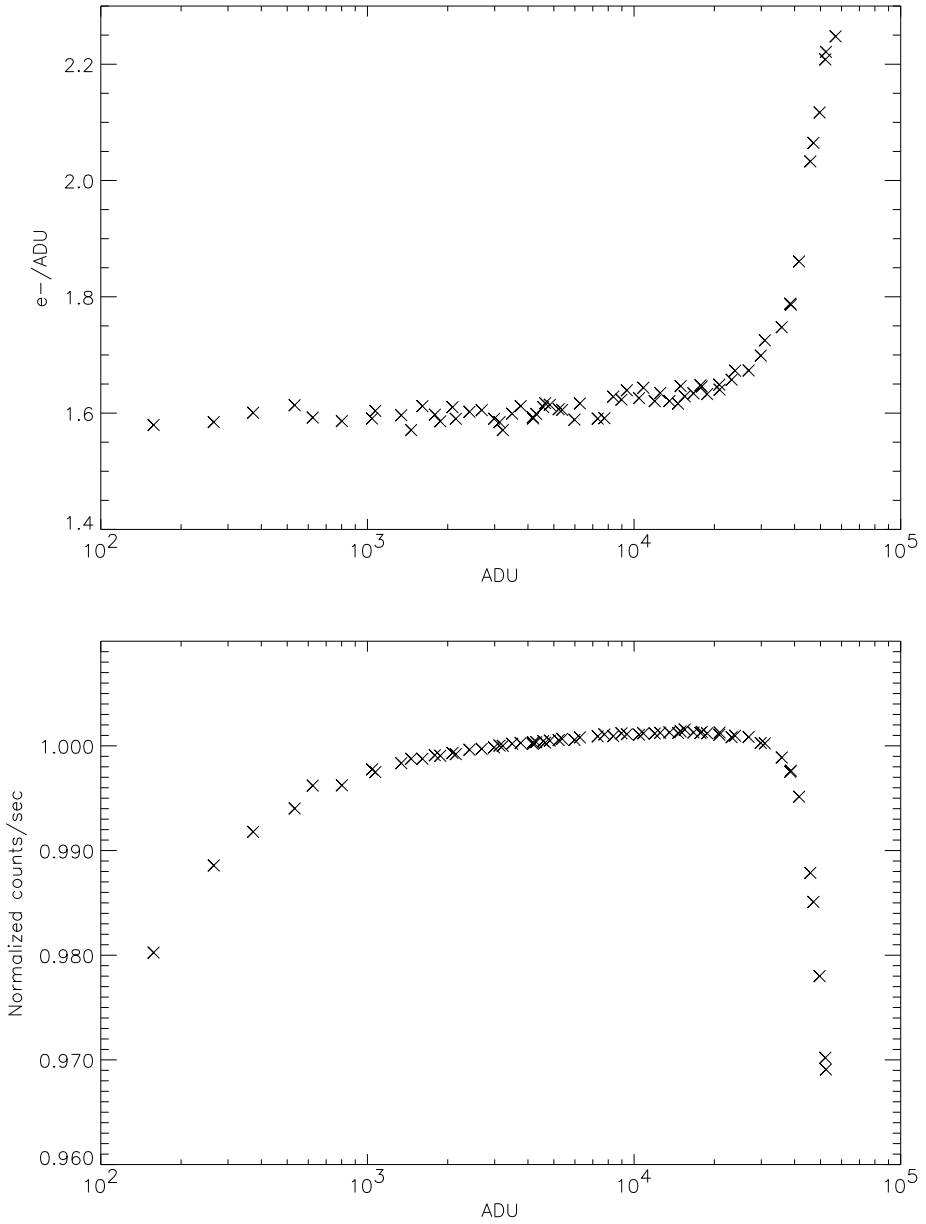

Figure 7: *Top:* Gain versus exposure level measured from noise statistics for amplifier B in low-gain mode. *Bottom:* A plot of ADU per second versus total exposure time, corrected for shutter delay. Data is again for amplifier B in low-gain mode.

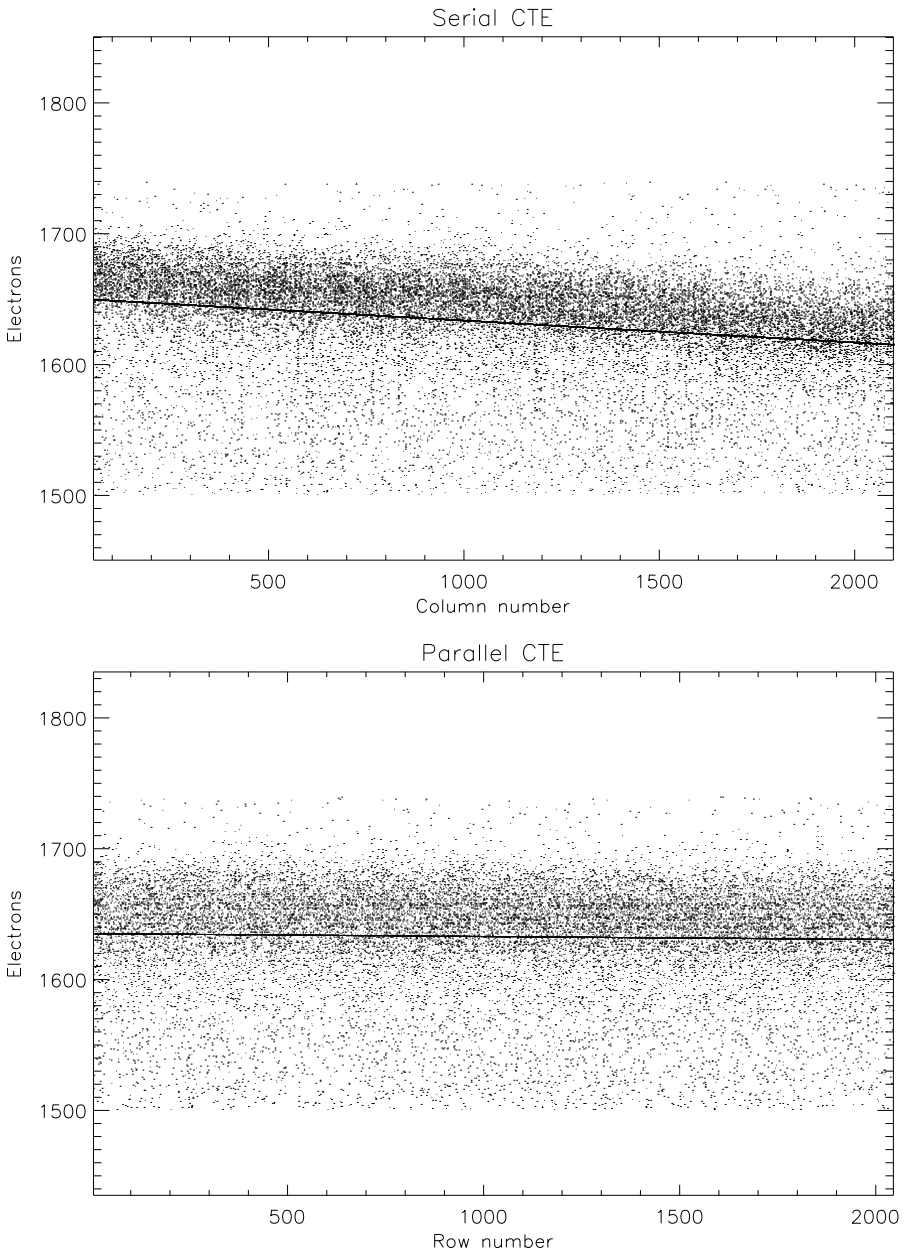

Figure 8: Plot of ^{55}Fe K-α peak counts versus row and column position, used for measuring CTE. The gradient along the rows shows a slight loss during serial transfers, while parallel shifts are near perfect.

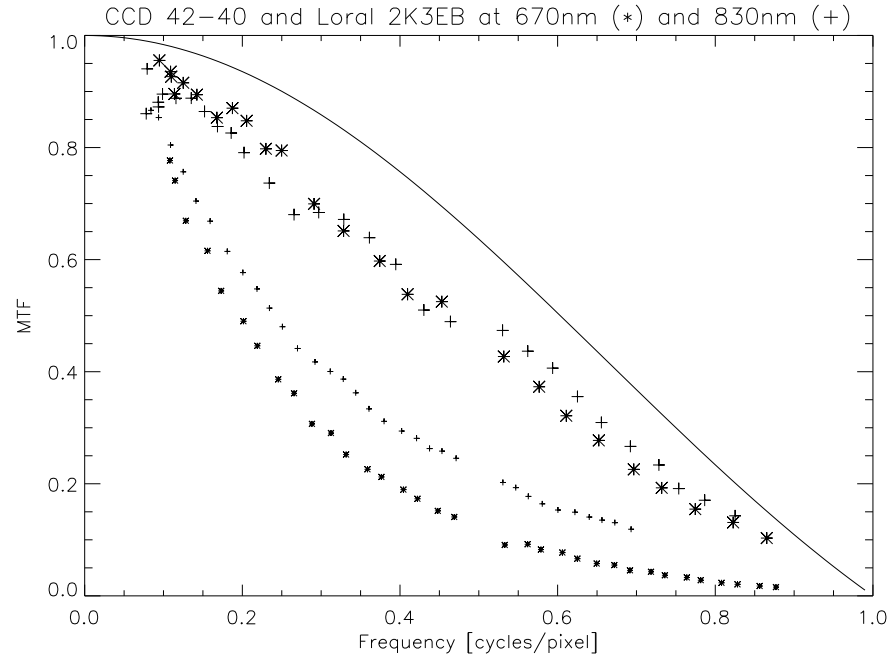

Figure 9: The two sets of large symbols show MTF measurements for the new CCD. Stars represent 670nm illumination and plusses 830nm. The smaller symbols show the same measurements for the previous Loral CCD on ALFOSC. The E2V has by far superior MTF, with little colour dependence.

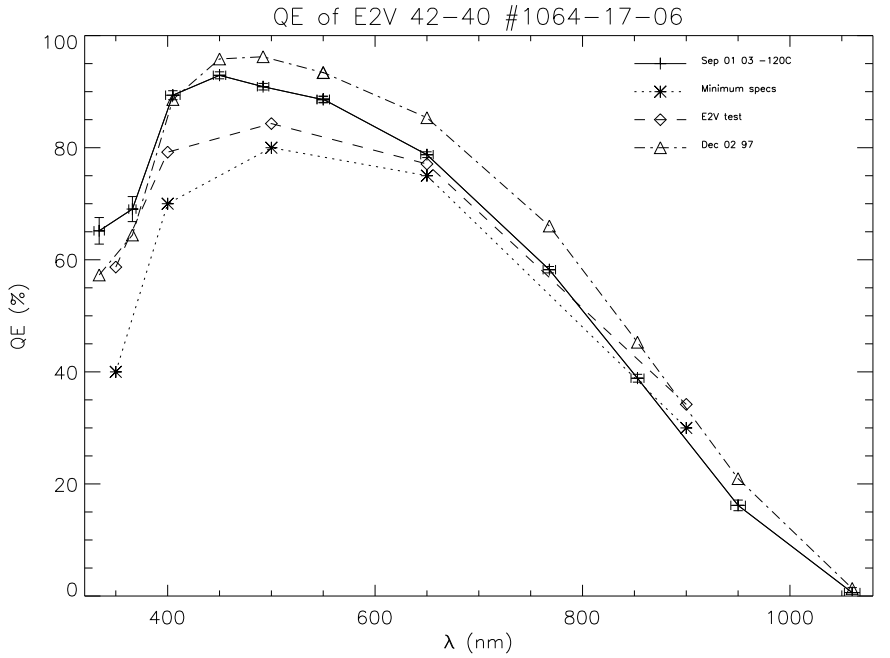

Figure 10: Quantum efficiency versus wavelength for the CCD42-40 at $-120°C$ (full drawn with bars). Also shown are E2V minimum specifications (stars) and test data (diamonds) at $-30°C$. QE of Loral CCD (triangles) is shown for comparison. The vertical bars shows the Pixel Response Non-Uniformity.

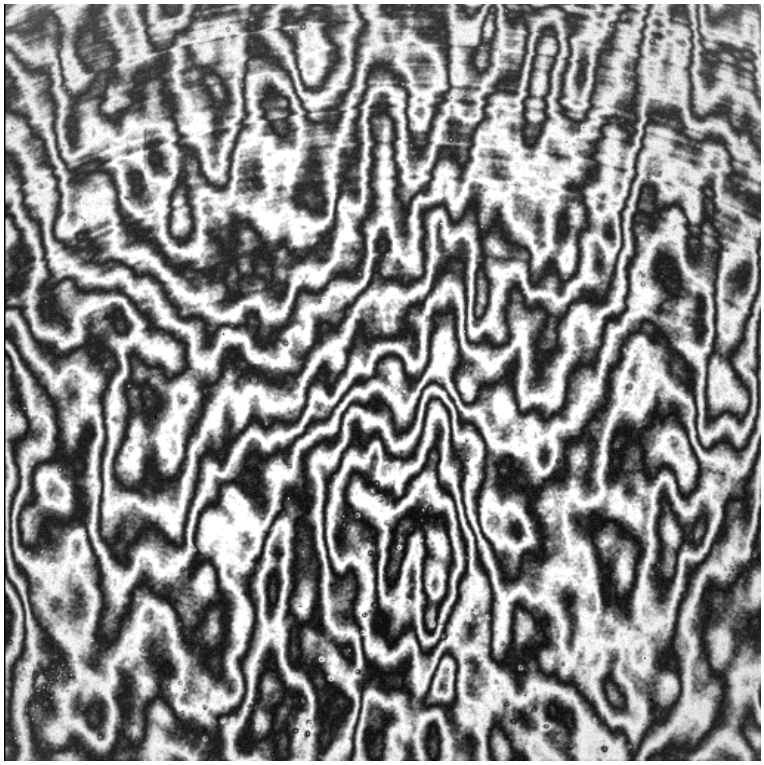

Figure 11: Fringing from 830nm laser illumination. The greyscale cuts are set to ±25% of the median level.

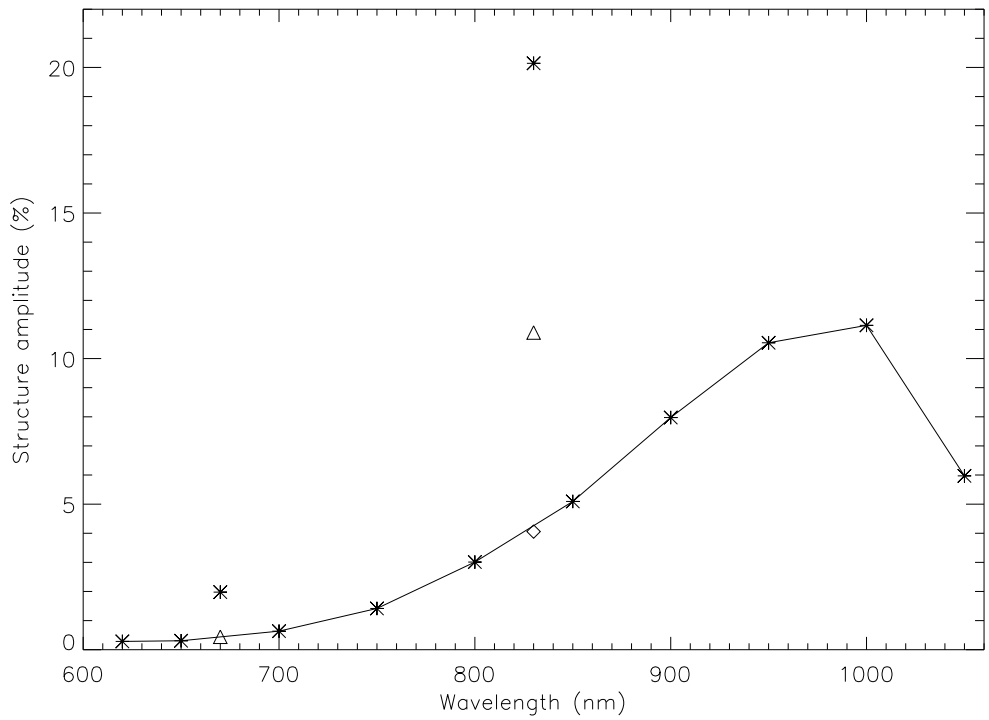

Figure 12: Fringe amplitude dependence on wavelength. Stars are for the E2V 42-40 Other symbols are for Loral CCDs. The curves are for monochromator data, and the isolated points laser data.

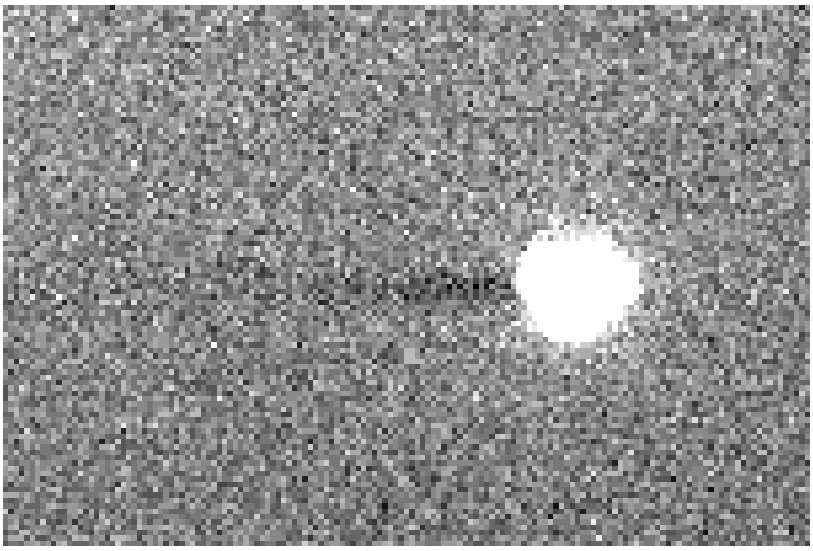

Figure 13: Dark tail from 40 KADU star, read out through amplifier B. The counts in the tail drops by about 10 ADU.

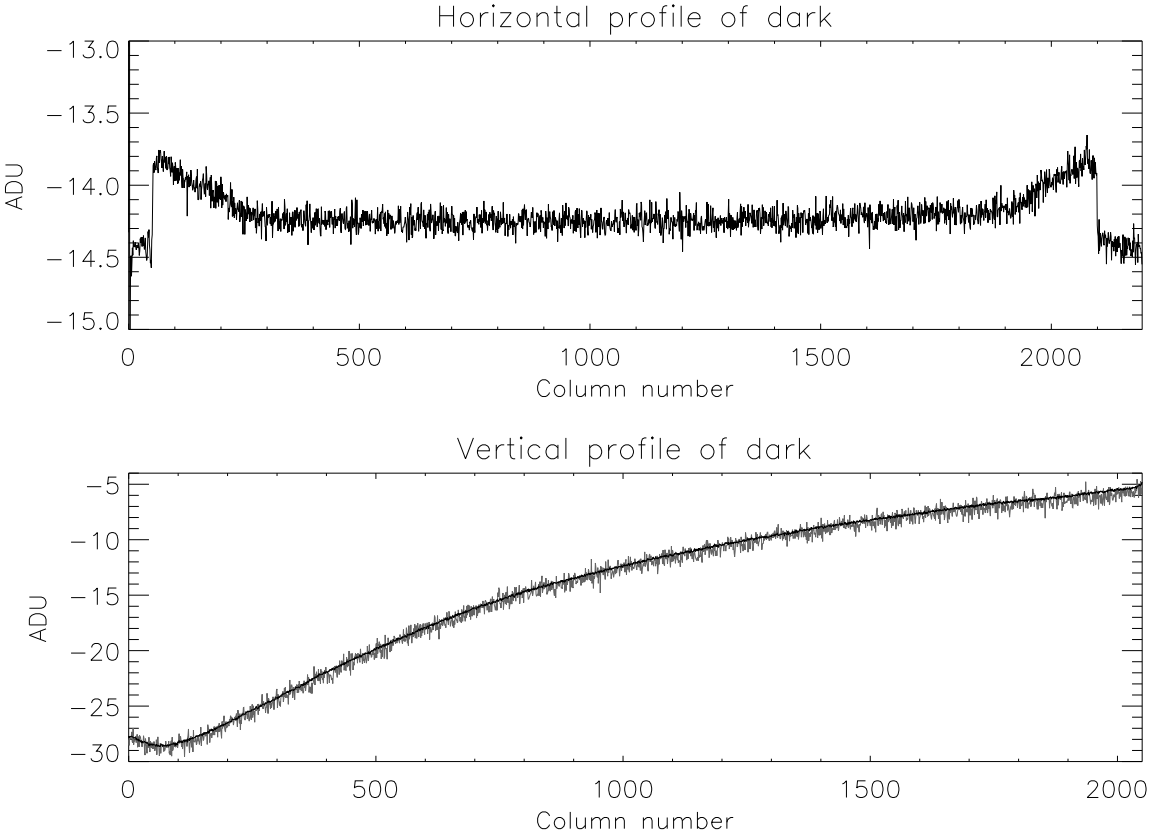

Figure 14: Horisontal and vertical profiles of the combination of several 1800sec dark exposures. In the horisontal profile, 50 pixels on each side of the imaging area trace the bias level, and on the right side further 50 pixels of artificial overscan are created by continued read-out beyond the length of the serial register. In the vertical profile, the narrow black graph is the dark level and the noisier grey graph is the overscan level.